Seventh International Conference on Computational Fluid Dynamics (ICCFD7), Big Island, Hawaii, July 9-13, 2012

ICCFD7-2106

A Level Set Based Method to Simulate Contact Line Motion and Dynamic Contact Angles for Multiphase Flow

G. Della Rocca* and G. Blanquart*
Corresponding author: gdr@caltech.edu

* Department of Mechanical Engineering
California Institute of Technology, Pasadena, CA.

June 29, 2012

Abstract: While various models for slip at a contact line between two fluids and a wall have been proposed, most require that the slip length of the model be sufficiently resolved in order to achieve convergence. This limitation makes the problems expensive computationally. In this study, a new model is proposed to capture the microscopic surface forces in macroscopic filtered Navier Stokes equations. An additional volumetric source term is added to the Navier Stokes equation while a simple model of shear stress is used for the viscous dissipation at the contact line. The terms are coupled to the levelset method for tracking the interface via the fluid dynamics code NGA. The final results show good comparison to theoretical work by Cox [1], however there is a grid dependence of the slip length in the current implementation.

Keywords: Level Set Methods, Multiphase Fluid Flow, Contact Line Dynamics

1 Introduction

Contact line motion is an element in many industrial and natural processes over a large range of length scales. At large length scales and high Reynolds (Re) numbers, droplet shearing is important to prevent icing of wind turbine blades and to enhance heat transfer in boiling processes. At smaller scales, capillary driven flow dominates the fluid behavior for coating technology, ink jet printing, enhanced oil recovery, biological processes, and polymer electrolyte fuel cells. In all these cases, the contact line motion can be used to optimize performance by maximizing or inhibiting the spread and transport of liquids. This paper focuses on developing a computational framework for capillary dominated flows, specifically at low Reynolds (Re) and capillary numbers (Ca) for two reasons: 1) there exist numerous theoretical studies for such a model to be compared against in this regime and 2) once the fundamental physics of the capillary forces at the contact line have been incorporated in the numerical method, it can be potentially used for higher Re where comparatively few models exist.

The moving contact line problem arises from a singularity in the shear stress at the contact line where the two fluids meet the solid [2, 3]. At steady state for flow in a channel, the interface between the two liquids must move with uniform velocity U. However, the classic no slip condition implies the fluid particles must have no velocity next to the wall. This discontinuity in velocity is the origin of the singular shear stress. The approaches to resolve this singularity fall into two broad categories [4]: a hydrodynamic, macroscale picture emphasizing viscous dissipation and a molecular-kinetic, microscale view focusing on the attachment and deattachment of fluid particles at the contact line. For the purposes of non-molecular simulations, the length scale of the second viewpoint is not resolved, so that viewpoint will not be discussed here. In order

to relieve the stress singularity, the most common method is to impose some form of a slip condition in the vicinity of the contact line. One example is the Navier slip condition

$$U_{slip} = s\frac{\partial U}{\partial n} \tag{1}$$

which states that the slip velocity U_{slip} is equal to the velocity gradient perpendicular to the wall multiplied by the slip length s where n is the direction perpendicular to the wall [5, 6, 7]. This condition has been shown to be accurate for low shear rates using molecular dynamics simulations [8, 9].

However, this condition cannot be used alone because it provides no means for a droplet at rest to achieve its static equilibrium contact angle θ_s. Indeed, any circular arc (constant curvature) is an equilibrium solution. As such, slip conditions must be supplemented with a contact line law which connects the velocity at the contact line to a given angle [10]. The simplest form is to force the contact angle to a static value, θ_s. However, this choice does not allow the existence of the dynamic contact angle seen experimentally [11]. Dynamic contact angle laws have been formulated such as the asymptotic analysis of Cox [1] for the macroscopic contact angle θ_D with small Ca and Re. In that study, only smooth, chemically homogeneous surfaces were considered (i.e. no contact angle hysteresis [3]) and the Ca was assumed to be very small in both fluids such that perturbation expansions could be used. The fluid region is broken into three distinct length scales for the analysis: one at slip length (microscopic) scale s, another at the macroscopic length scale R, and a third at a mesoscopic length scale in between for matching. The no-slip condition is applied in the larger two regions all along the wall, while in the microscopic region a composite slip condition is applied with no-slip far away from the line and slip immediately at the line. Due to the matching procedure, the exact form of the slip law is not relevant, only the length scale s is. In the smallest length scale region, it is assumed that there is a fixed angle at the wall regardless of the flow. Since it is fixed, this angle at the wall must be the static contact angle θ_s. The final result is an implicit expression for the dynamic contact angle θ_D as a function of the Ca, the ratio of the microscopic and macroscopic length scales $\epsilon = \frac{s}{R}$, and the ratio of the fluid viscosities λ.

$$g(\theta_D) = g(\theta_s) + Caln(\epsilon^{-1}) \tag{2}$$

$$g(\theta) = \int_0^\theta \frac{1}{f(\theta)}\partial\theta \tag{3}$$

$$f(\theta) = \frac{2sin\theta((\lambda^2(\theta^2 - sin^2\theta) + 2\lambda(\theta(\pi-\theta) + sin^2\theta) + ((\pi-\theta)^2 - sin^2\theta))}{\lambda(\theta^2 - sin^2\theta)((\pi-\theta) + sin\theta cos\theta) + ((\pi-\theta)^2 - sin^2\theta)(\theta - sin\theta cos\theta)} \tag{4}$$

Several numerical experiments have confirmed these results [8, 12]. A version was later developed for larger Reynolds numbers ($Re > 1$); this form however was derived for vacuum as the displaced fluid and thus is only applicable if $\lambda << 1$. In some studies, the angle is calculated from Eq. (2) and then the boundary is forced to this angle [13, 14].

These contact line conditions for slip and angles need to be coupled with an appropriate numerical method for simulating multiphase flows. Three commonly used methods are the volume of fluid (VOF) method [15, 16], the front tracking method [17], and the levelset method [18]. In the VOF approach, a scalar is assigned to each grid cell that represents the liquid volume fraction in the cell. Using conservative transport methods, VOF methods discretely conserve mass in the system. However, reconstructing the interface between the fluid, and thereby computing the interface curvature and normals, is non-trivial. Since the flows in the regime examined are dominated by capillary forces, even small errors in curvature will incorrectly deform the interface. In the front tracking approach, an unstructured mesh of points are placed on the interface and they are transported in a Lagrangian fashion to determine the location of the interface. These methods have difficulty handling topological changes such as merging profiles and require frequent mesh rearrangements as tracking points get too close or too far apart from one another. Level set methods represent the interface as an isocontour of a smooth function ϕ. The scalar values of ϕ are transported using Eulerian transport schemes. This approach is advantageous for low Ca problems because it is simple to calculate accurately curvature and naturally handles topology changes. The level set approach, however, does not have any discrete mass conservation and hence is particularly susceptible to mass loss/addition. Several modifications

have been proposed to alleviate this problem: particle level set methods [19], combined volume of fluid and level set methods [20], hyperbolic tangent level set functions [21], and constrained reinitialization [22].

In this study, a level set method is chosen to track the interface of the fluids due to its simple, accurate calculations of curvature and its natural handling of topological changes for future studies of drop detachment and reattachment. In section 2, the governing equations and numerical implementation is discussed. These equations are then applied to the case of Poiseuille flow with the Navier slip condition and fixed contact angle θ_s in section 3. These simulations show that unless the slip length is completely resolved the interface shape does not appear to converge, agreeing with the work of Afkhami *et. al.* [14]. In section 4, volumetric source terms are examined for the missing physics in filtered simulations and a simple geometry-based model is proposed that provides an additional pressure jump at the contact line. In section 5, the model is used to generate θ_D as a function of Ca for the model. The results of the proposed numerical model are compared to the theoretical work of Cox [1].

2 Computational Framework

2.1 Governing Equations

The two fluids are assumed to be immiscible, incompressible, Newtonian fluids. The equations of motion are:

$$\frac{\partial \rho \underline{u}}{\partial t} + \nabla \cdot (\rho \underline{u} \otimes \underline{u}) = \nabla \cdot (-p \underline{\underline{I}} + 2\mu \underline{\underline{D}}) + \underline{b} \tag{5}$$

$$\nabla \cdot \underline{u} = 0$$

where $\underline{u}$ is the velocity vector, $\underline{b}$ are the volumetric source terms, ρ is the density of the fluid phase, μ is the kinematic viscosity, $\underline{\underline{I}}$ is the unit tensor, and $\underline{\underline{D}}$ is the symmetric deformation tensor defined by

$$\underline{\underline{D}} = \frac{1}{2}(\nabla \underline{u} + \nabla \underline{u}^T)$$

For the small length scales considered, the Bond number is very small, so any body forces due to gravity may be neglected. In the absence of the additional body forces, $\underline{b} = 0$. In the levelset framework, the interface between fluids 1 and 2 is represented by the isocontour $\phi = 0$ [18]. At the interface, both normal velocities and tangential velocities are continuous

$$[\underline{u}] = 0 \tag{6}$$

where the square brackets represent a jump between fluid 1 and 2. Let $\underline{t}_1$, $\underline{t}_2$, and $\underline{n}$ be the two tangential vectors and normal vector to the interface respectively. The tangential stress at the interface must be continuous

$$[\underline{t}_1 \cdot (-p \underline{\underline{I}} + 2\mu \underline{\underline{D}}) \cdot \underline{n}] = [\underline{t}_2 \cdot (-p \underline{\underline{I}} + 2\mu \underline{\underline{D}}) \cdot \underline{n}] = 0 \tag{7}$$

and the jump in normal stress is given by Laplace's formula [23]

$$[p] - [2\mu \hat{n} \cdot \nabla \underline{u} \cdot \hat{n}] = \sigma \kappa \tag{8}$$

where σ is the coefficient of surface tension and κ is the curvature of the interface. The levelset variable ϕ is advected using the scalar advection equation

$$\frac{\partial \phi}{\partial t} + \underline{u} \cdot \nabla \phi = 0 \tag{9}$$

Let fluid 1 be when $\phi < 0$ and fluid 2 be when $\phi > 0$. The curvature can then be calculated from the normals of ϕ

$$\underline{n} = -\frac{\nabla \phi}{|\nabla \phi|}, \quad \kappa(\phi) = \nabla \cdot \left(\frac{\nabla \phi}{|\nabla \phi|} \right) \tag{10}$$

and the density of the fluid is treated in a sharp manner based on the Heaviside function H

$$\rho = \rho_2 H(\phi) + \rho_1 (1 - H(\phi)) \tag{11}$$

$$H(\phi) = \begin{cases} 1, & \phi \geq 0 \\ 0, & \phi < 0 \end{cases} \tag{12}$$

2.2 Numerical Methods

All calculations were carried out in the NGA framework; for a detailed description of the methods see Desjardins *et. al.* [24, 25]. The governing equations are discretized using centered finite differences and the field variables are stored on a staggered mesh. The single phase incompressible flow solver uses an iterative projection method to calculate the velocity [26] and an algebraic multigrid (AMG) solver for the pressure poisson equation. The level set function ϕ is transported and held constant during each solve of the velocity field. The spectrally refined interface (SRI) scheme [25] and the modified Hamilton-Jacobi equation of Hartmann *et. al.* [22] are used for the transport of the level set function and its reinitialization respectively. The curvature of the level set function ϕ is calculated using a second order least square fit polynomial with a stencil of three data points in each direction. The jump term in pressure (16) is applied as a source term of velocity using the ghost fluid method (GFM) [25, 27].

While the density is treated as a sharp discontinuity, viscosity is taken as a harmonic combination of μ_1 and μ_2

$$\mu = \frac{\mu_1 \mu_2}{\mu_1 \theta + \mu_2 (1 - \theta)} \tag{13}$$

based off a height fraction θ to ensure continuity of the tangential shear stress [28, 29]. For a staggered grid, the height fraction at cell faces is

$$\theta_{i+1/2,j} = \begin{cases} 1 & \phi_{i+1,j} \geq 0 \text{ and } \phi_{i,j} \geq 0 \\ 0 & \phi_{i+1,j} \leq 0 \text{ and } \phi_{i,j} \leq 0 \\ \frac{\phi^+_{i+1,j} + \phi^+_{i,j}}{|\phi_{i+1,j}| + |\phi_{i,j}|} & \text{otherwise} \end{cases} \tag{14}$$

and for cell vertices

$$\theta_{i+1/2,j+1/2} = \begin{cases} 1 & \phi_{i+1,j} \geq 0,\ \phi_{i,j} \geq 0,\ \phi_{i,j+1} \geq 0, \text{ and } \phi_{i+1,j+1} \geq 0 \\ 0 & \phi_{i+1,j} < 0,\ \phi_{i,j} < 0,\ \phi_{i,j+1} < 0, \text{ and } \phi_{i+1,j+1} < 0 \\ \frac{\phi^+_{i+1,j} + \phi^+_{i,j} + \phi^+_{i,j+1} + \phi^+_{i+1,j+1}}{|\phi_{i+1,j}| + |\phi_{i,j}| + |\phi_{i,j+1}| + |\phi_{i+1,j+1}|} & \text{otherwise} \end{cases} \tag{15}$$

The height fraction can be considered as the amount of fluid 2 that would be present in a VOF framework. The "+" superscript is a shorthand notation for $\phi^+ = max(\phi, 0)$. This formulation differs from that of Kang *et. al.* [28] in that the viscous jump terms are not included; according to Kang excluding these terms would only result in a small amount of numerical smearing. Since the viscosity field is sharp but continuous using Eq. (13), Equation (8) is reduced to

$$[p] = \sigma \kappa \tag{16}$$

This jump condition is then applied in the ghost fluid method.

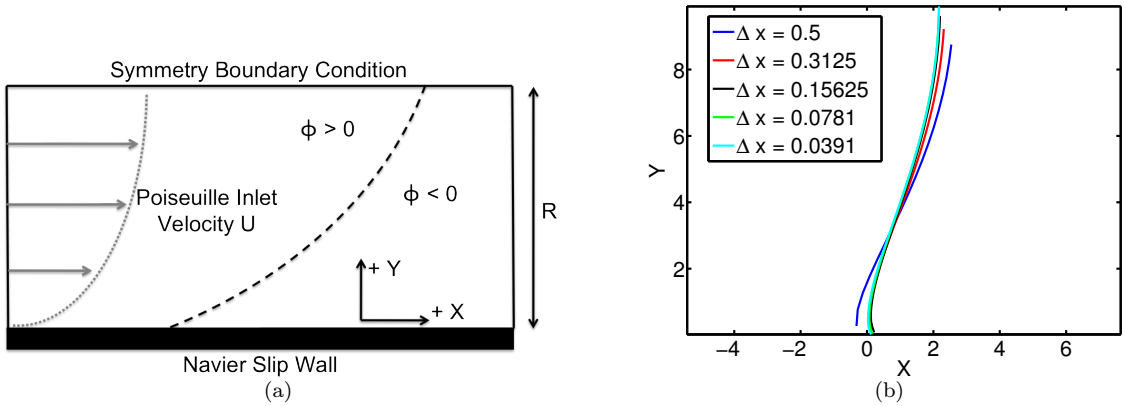

Figure 1: (a) Channel geometry for simulations with the Navier slip boundary condition at the wall. (b) Solution interface profiles at steady state for several different grid resolutions.

3 Fully-Resolved Poiseuille Flow with a Navier Slip Condition

The simplest case of multiphase flow in a two-dimensional channel is examined with one fluid displacing another. The test geometry is shown in Fig. 1(a). Half of the channel is created by applying a symmetry boundary condition on the top of the domain and a Navier slip condition at the wall. The inlet velocity is a Poiseville type velocity profile and the outlet has an outflow boundary condition. As long as the interface is far from the outlet, the outflow boundary condition has a negligible effect on the flow. The numerical grid is composed of square cells and only this type of cell will be examined here.

From dimensional analysis, the relevant dimensionless groups are λ, ϵ, the ratio of densities η, Re, and Ca. The Reynolds number based on the radius of the channel and the properties of the more viscous fluid is chosen as 1: this choice ensures that the inertial effects are small in the flow. Furthermore, since the Re is small, the solution is approximately in the Stokes flow regime. Since Cox's analysis used the Stokes equation for the macroscopic portion of the solution [1] and the ultimate goal of this paper is a comparison to Cox's theory, the parameter can be excluded from the analysis. For numerical stability and ease of simulation, $\eta = 1$ in all the simulations. R is set to a non-dimesional value of 10. As mentioned previously, a slip condition and contact line angle condition must supplement the multiphase fluid flow solver; the slip condition chosen at the wall is the Navier slip condition Eq. (1) and the contact line angle is fixed at $\theta_s = 60^0$.

All of the simulation profiles were run sufficiently long to achieve steady state and a constant velocity U in the x-direction along the interface profile. Several profiles were run at different resolutions for $Ca = 0.1$ and with a slip length s = 0.2 (Fig. 1(b)). The profiles appear to have a consistent shape so long as the grid resolution Δx is smaller than s. This agrees with the results of Afkhami *et. al.* [14] where the authors saw a similar convergence as long as $\Delta x < s$. As noted by those authors, such a resolved simulation is often prohibitively computationally expensive.

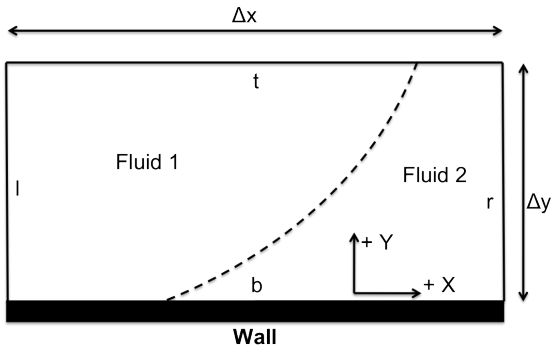

Figure 2: Individual interface cell over which the volumetric equations are examined.

4 Filtered Navier-Stokes Equations

Since most slip lengths are much smaller than the macroscopic length scales of a system, it is often impossible to perform fully resolved numerical simulations. In order to alleviate this problem, a new numerical framework is proposed. The original equations are filtered and two unclosed terms are identified which need to be modeled. These terms from the additional forces can be added $\underline{b}$ in Eq. (5) and applied only at cells adjacent to the contact line.

4.1 Derivation of the Filtered Equations

In this section, the filtered Navier-Stokes equations are derived by considering a box filter of size Δx, Δy. In other words, the equations are averaged over a given volume. For simplicity, only the two-dimensional case is explored here although an extension to three-dimensions is straightforward.

Assumption 1: Assume ρ and μ are constant on each side of the interface. This assumption is perfectly valid for incompressible fluids.

Let the fluid on the left side of the interface be fluid 1 and the right fluid 2 (Fig. 2). The sides of the box filter will be denoted by subscripts (l,r,t,b). Each term needs to be integrated over the volume. The volume integration is defined as

$$\overline{\Psi} = \frac{1}{V}\iiint_V \Psi \mathrm{dV} = \frac{1}{V}\left(\iiint_{V_1} \Psi \mathrm{dV} + \iiint_{V_2} \Psi \mathrm{dV}\right)$$

where Ψ represents any quantity. Integrating and applying the divergence theorem to Eq. (5),

$$\frac{\partial \overline{\rho \underline{u}}}{\partial t} + \frac{1}{V}\oint_S (\rho \underline{u} \otimes \underline{u}) \cdot \mathrm{dS} = -\frac{1}{V}\oint_S P \mathrm{dS} + \frac{1}{V}\oint_S 2\mu \underline{\underline{D}} \cdot \mathrm{dS}$$

At this point, a new terminology called the LHS is introduced into the equation and begins with the current left hand side terms. This quantity will contain all the terms that are modeled correctly in the macroscopic sense and as such do not require closure. Any additional terms that need to be added to a macroscale numerical scheme or modified terms will be kept on the right. In the new notation,

$$LHS = -\frac{1}{V}\oint_S P \mathrm{dS} + \frac{1}{V}\oint_S 2\mu \underline{\underline{D}} \cdot \mathrm{dS}$$

Breaking down the integral into x and y components,

$$\begin{aligned} LHS_x = & \frac{1}{\Delta x \Delta y} \int_0^{\Delta y} (P_l - P_r) \mathrm{dy} + \\ & \frac{1}{\Delta x \Delta y} \int_0^{\Delta y} \left(2\mu \frac{\partial u}{\partial x}_r - 2\mu \frac{\partial u}{\partial x}_l \right) \mathrm{dy} + \\ & \frac{1}{\Delta x \Delta y} \int_0^{\Delta x} \left[\mu (\frac{\partial v}{\partial x} + \frac{\partial u}{\partial y})_t - \mu (\frac{\partial v}{\partial x} + \frac{\partial u}{\partial y})_b \right] \mathrm{dx} \end{aligned} \tag{17}$$

$$\begin{aligned} LHS_y = & \frac{1}{\Delta x \Delta y} \int_0^{\Delta x} (P_b - P_t) \mathrm{dx} + \\ & \frac{1}{\Delta x \Delta y} \int_0^{\Delta x} \left(2\mu \frac{\partial v}{\partial y}_t - 2\mu \frac{\partial v}{\partial y}_b \right) \mathrm{dx} + \\ & \frac{1}{\Delta x \Delta y} \int_0^{\Delta y} \left[\mu (\frac{\partial v}{\partial x} + \frac{\partial u}{\partial y})_r - \mu (\frac{\partial v}{\partial x} + \frac{\partial u}{\partial y})_l \right] \mathrm{dy} \end{aligned} \tag{18}$$

Only the x-direction equation (17) is analyzed. The y-direction equation can be shown to include no unclosed terms and thus is already correct in the macroscopic sense. Applying the directional averages

$$\overline{a}^x = \frac{1}{\Delta x} \int_0^{\Delta x} a \mathrm{dx}$$

$$\overline{a}^y = \frac{1}{\Delta y} \int_0^{\Delta y} a \mathrm{dy}$$

to equation Eq. (17)

$$\begin{aligned} LHS_x = & \frac{1}{\Delta x} \underbrace{(\overline{P_l}^y - \overline{P_r}^y)}_{A} \\ & + \underbrace{\frac{2}{\Delta x} \overline{(\mu \frac{\partial u}{\partial x})_r}^y - \frac{2}{\Delta x} \overline{(\mu \frac{\partial u}{\partial x})_l}^y}_{B} \\ & + \underbrace{\frac{1}{\Delta y} \overline{(\mu \frac{\partial v}{\partial x})_t}^x + \frac{1}{\Delta y} \overline{(\mu \frac{\partial u}{\partial y})_t}^x}_{C} \\ & \underbrace{- \frac{1}{\Delta y} \overline{(\mu \frac{\partial v}{\partial x})_b}^x - \frac{1}{\Delta y} \overline{(\mu \frac{\partial u}{\partial y})_b}^x}_{D} \end{aligned} \tag{19}$$

Assumption 2: The averaging volume is much bigger than the slip length, $s << \Delta x, \Delta y$.

Velocity terms at top, left, and right of the cell (Fig. 2) are therefore outside of the microscopic region and have no need to be modeled. Therefore, Terms B and C of Eq. (19) can therefore be added to LHS. Terms A and D need to be modeled to account for the microscale interactions at the contact line. Since the wall is impenetrable the value of v is everywhere zero so $\frac{\partial v}{\partial x} = 0$. Equation (19) reduces to

$$LHS_x = \frac{1}{\Delta x} \underbrace{(\overline{P_l}^y - \overline{P_r}^y)}_{A} - \frac{1}{\Delta y} \underbrace{\overline{(\mu \frac{\partial u}{\partial y})_b}^x}_{D} \tag{20}$$

Term A represents the jump term in Laplace's equation due to the presence of the surface, and Term D represents the effective friction law at the wall to account for the enhanced viscous dissipation.

Assumption 3: $\nabla\overline{P}^y$ is the same on the left and right hand faces of the interface. This assumption is inherent in the GFM.

Using the GFM and this first order approximation for the gradient of $\overline{P}^y$, the pressure difference can be written as

$$\overline{P_l}^y - \overline{P_r}^y = -\nabla\overline{P}^y\Delta x + [\overline{P}^y]$$

where $[a]$ signifies a jump in the variable a across the interface between the fluids. Applying the Laplace equation (16) for the jump in pressure,

$$\overline{P_l}^y - \overline{P_r}^y = -\nabla\overline{P}^y\Delta x + \sigma\frac{1}{\Delta y}\int_0^{\Delta y}\kappa(y)\mathrm{dy}$$

The averaged curvature can be written as the sum of the curvature determined by the filtered levelset field ($\overline{\phi}$) and an unresolved, sub-filter, deviation term (κ_{unr}),

$$\overline{\kappa} = \frac{1}{\Delta y}\int_0^{\Delta y}\kappa(y)\mathrm{dy} = \kappa(\overline{\phi}) + \kappa_{unr}$$

$$\overline{P_l}^y - \overline{P_r}^y = -\nabla\overline{P}^y\Delta x + \sigma(\kappa(\overline{\phi}) + \kappa_{unr}) \tag{21}$$

κ_{unr} accounts for the interface curvature "lost" during the filtering operation and represents a restoration pressure to the thermodynamic equilibrium contact angle. Applying Eq. (21) to Eq. (20),

$$LHS_x = \underbrace{\frac{1}{\Delta x}\left(-\nabla\overline{P}^y\Delta x + \sigma\kappa(\overline{\phi})\right)}_{E} + \frac{1}{\Delta x}\sigma\kappa_{unr} - \frac{1}{\Delta y}\overline{(\mu\frac{\partial u}{\partial y})_b}^x$$

Since Term E only involves macroscale quantities, it can now be moved over into LHS_x. This leaves

$$LHS_x = \underbrace{\frac{1}{\Delta x}\sigma\kappa_{unr}}_{F} - \underbrace{\frac{1}{\Delta y}\overline{(\mu\frac{\partial u}{\partial y})_b}^x}_{D} \tag{22}$$

Two unclosed terms remain and are modeled in the following sections.

4.2 Unresolved Curvature - Term F

In the asymptotic analysis of Cox [1], there was always a microscopic fixed contact angle θ_s in the smallest length scale region. Using this idea as motivation,

Assumption 4:The contact angle at the wall is always θ_s and the transition to this angle happens over a distance Δy from the wall (Fig. 3(a)).

Assuming a constant curvature transition (i.e. the smoothest possible case) between the angle θ at the cell center and the angle θ_s at the wall (Fig. 3(b)), the pressure jump from geometry across the interface takes the form

$$\sigma\kappa_{unr}(y) = \sigma(\frac{cos(\theta) - cos(\theta_s)}{\Delta y}) \tag{23}$$

for any values of θ, θ_s.

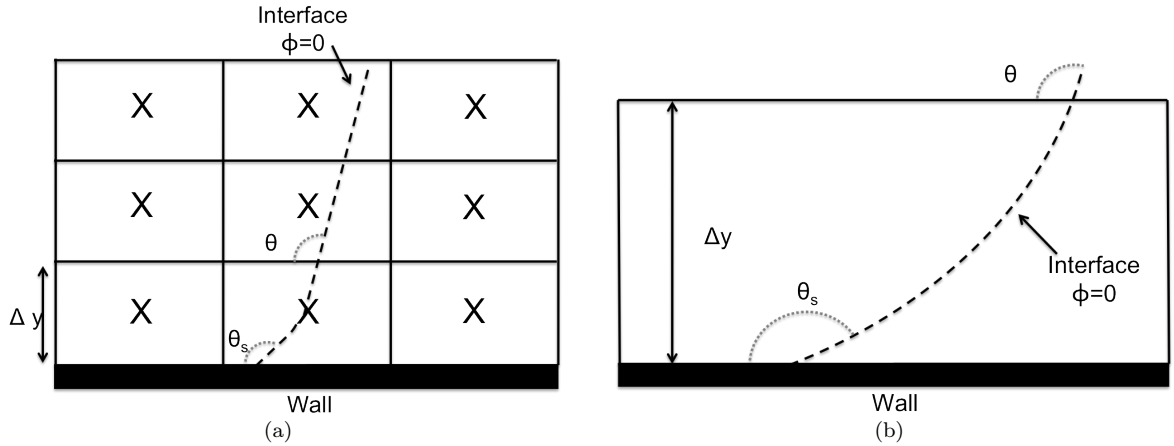

Figure 3: (a)Diagram of computational grid with angle θ at the cell centers and θ_s at the wall in the unresolved region of the domain. (b) Subgrid smooth transition between the angles θ and θ_s over a length scale L.

A similar result can be derived by considering the unbalanced Young's force [30] spread over the cell. The model can be further expanded to include pinning forces by using the hysteresis contact angles θ_A, θ_R instead of θ_s [31] or limiter on the minimum magnitude of $\sigma\kappa_{unr}$.

4.3 Shear Model - Term D

Assumption 5: To approximate the shear stress at the wall, an appropriate slip condition needs to be considered at the contact line. In this case, the Navier slip condition

$$\frac{\partial u}{\partial y} = \frac{u}{s}$$

was assumed to be the boundary condition at the wall in the vicinity of the contact line only.

While this assumption may seem to be restrictive, previous studies have implied that all slip conditions appear the same macroscopically with differences appearing in the choice of fitted constants for the model [1, 12].

Let u^* be the velocity at the contact line. Far away from the contact line ($\frac{x}{s} >> 1$), the velocity at the wall is expected to achieve a value u_∞which is independent of the behavior at the contact line. A general form of the velocity along the wall can then be expressed as

$$u\left(\frac{x}{s}\right) = u_\infty + (u^* - u_\infty) f\left(\frac{x}{s}\right)$$

where $f(\frac{x}{s})$ is a function with the bounds

$$f(0) = 1, \quad f(\infty) = 0$$

Assumption 6: The flow geometry at the contact line is symmetric enough that a single $f\left(\frac{x}{s}\right)$ can be used for both sides of the flow.

Applying the Navier Slip condition and a height fraction θ [5, 32] to the approximate the split between fluids 1 and 2, Term D becomes

$$\overline{(\mu\frac{\partial u}{\partial y})_b}^x = \frac{u_\infty}{s}(\mu_1\theta + \mu_2(1-\theta)) + \frac{u^* - u_\infty}{s\Delta x}\left(\mu_1\int_0^{\frac{\theta x}{s}} f(t)\mathrm{dt} + \mu_2\int_0^{\frac{(1-\theta)x}{s}} f(t)\mathrm{dt}\right)$$

This equation implies that a suitable choice for the viscosity at the wall μ^* should be given by the linear average

$$\mu^* = \mu_1\theta + \mu_2(1-\theta)$$

This form of a "smeared" viscosity is different from the node-based harmonic viscosity expression used everywhere else in the domain Eq. (13). However, the previous expression by Sussman [29] did not consider a node located on a wall in the contact line region. This condition supplements the existing mixture rule for μ.

Without a specific form of the function $f(t)$, no additional evaluation of Term D can be accomplished. In the current work, a very simple model is used for term D, i.e. that the mean of the shear is equal to the shear of the mean. While this choice is may not be perfect, it provides a starting point for improvement.

Assumption 7: Term D can be expressed as

$$\overline{(\mu\frac{\partial u}{\partial y})_b}^x = \mu^*\overline{(\frac{\partial u}{\partial y})_s} \tag{24}$$

where $\overline{(\frac{\partial u}{\partial y})_s}$ is the value of shear rate provided by the macroscale simulation and hence is fully closed.

4.4 Summary

The filtered Navier-Stokes equations at the wall are identical to the original Navier-Stokes equations with the exception of the unresolved curvature term Term F. This term can be treated as a body force applied at the contact line. This value of $\underline{b}$ in Eq. (5) can be expressed as the vector for horizontal walls

$$\underline{b} = \begin{bmatrix} \sigma\frac{cos(\theta) - cos(\theta_s)}{\Delta x\Delta y}\delta_b \\ 0 \end{bmatrix}$$

where

$$\delta_b = \begin{cases} 1 & \text{interface cell on wall} \\ 0 & \text{otherwise} \end{cases}$$

5 Results

The Poiseuille flow simulation of section 3 is run again, however this time with a no slip condition at the wall (Fig. 4). In these iterations, Ca was varied as well to generate curves that can be compared to the analytical expressions of Cox [1].

5.1 Dynamic Contact Angle Calculation

In order to compare dynamic contact angles θ_D, a procedure must be established to calculate the angle from the interface shape. Since both We and Ca are small, the surface tension is the dominant effect and will cause the interface to be almost a circular arc. In most experimental studies, it is extremely difficult to image accurately the angle at the contact line. Instead, the circular nature of the interface is considered and fitted with an arc [11]. Then the dynamic contact angle θ_D can is calculated using

$$cos(\theta_D) = \frac{R}{R_c} \tag{25}$$

where R_c is the radius of the fitted arc and R is the distance from the wall to the arc's center. Following this example, the interface curve ($\phi = 0$) is extracted from the simulation results and an optimized least square

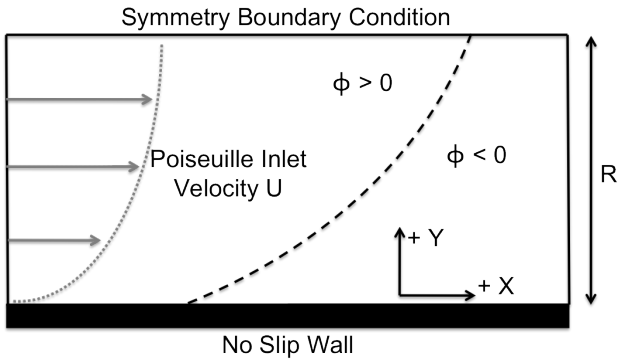

Figure 4: Channel geometry for simulations of dynamic contact angle with the no slip condition applied along the wall.

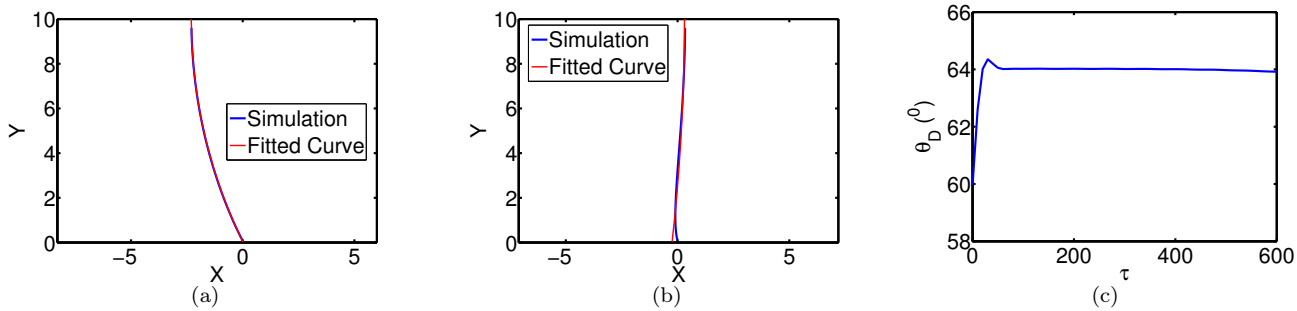

Figure 5: (a) Fitted circular arc to the interface for small deformation. (b) Fitted circular arc to the interface for large deformation. (c) Evolution of the contact angle from its static value $\theta_s = 60^o$ to the final dynamic value θ_D as a function of the dimensionless time τ.

fit is performed to a circular arc.

Generally, the fitted curves agree quite well for small deviations from the static contact angle (Fig. 5(a)). There are three main sources of error for the contact angle calculation: error from the optimizer E_{opt}, error in the profile oscillations in time E_{time}, and error if the interface profile is not a circular arc E_{fit}. The optimizer error E_{opt} is very small thanks to the constraints used in the optimizer. The evolution of the contact angle as a function of dimensionless time τ for a simulation run is shown in Fig. 5(c). Once steady-state is achieved, the predicted angle does fluctuate, but $E_{time} \sim 1^o$ (Note: these errors are worse at small Ca). Therefore, in most cases, these errors are small compared to the magnitude of the dynamic contact angle; so they will be excluded in the graphs to follow. For cases where the interface undergoes large deformations, specifically when it inverts itself, there appears to be a different curvature in the immediate vicinity of the wall that is not captured by the circular arc (Fig. 5(b)). This change is a local phenomenon and is also not captured by most measuring methods used in experiments; thus, its value will be excluded as well. However, it is important to note that these results imply that care must be taken when comparing to other works.

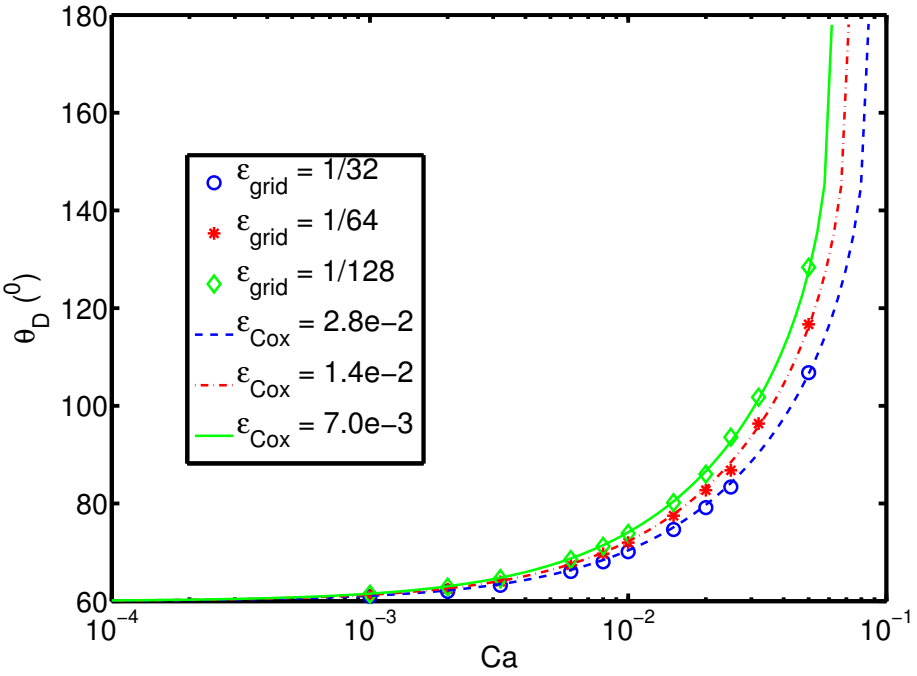

Figure 6: Dynamic contact angle θ_D as a function of the Ca from numerical simulations at three different grid resolutions for $\lambda = 1$.

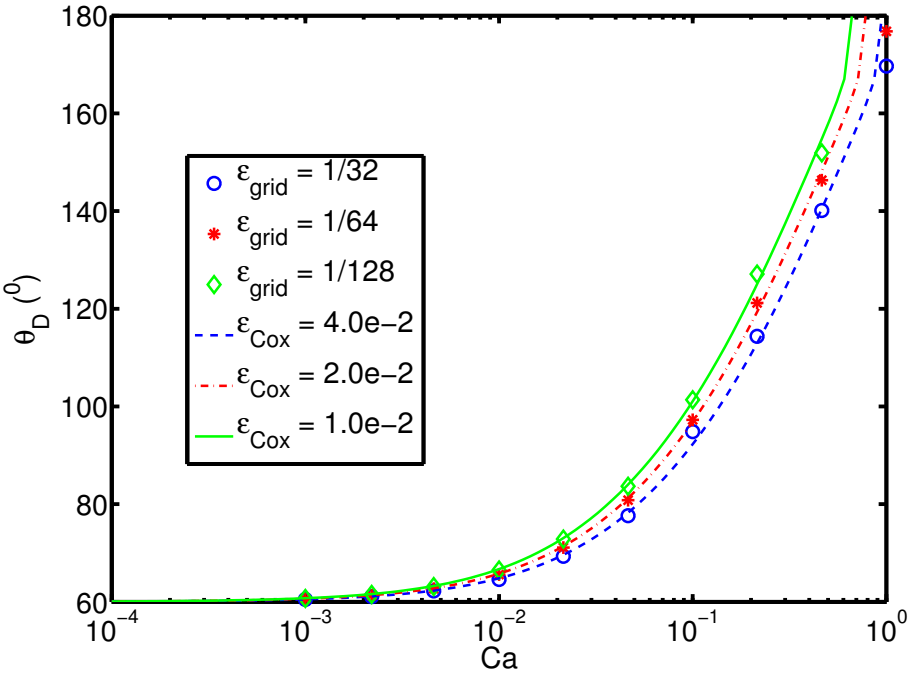

Figure 7: Dynamic contact angle θ_D as a function of the Ca from numerical simulations at three different grid resolutions for $\lambda = 10^{-3}$.

5.2 Simulated Dynamic Contact Angle

Simulations were performed for two different values of λ by varying Ca. Figure 6 shows the results for two very similar fluids, $\lambda = 1$, (such as oil and water). Figure 7 shows the results for $\lambda = 10^{-3}$ which is a closer approximation to a viscous liquid displacing a gas (such as water and air).

The curves show good agreement individually with Cox's theory. Since the slip length s does not appear anywhere in the filtered equations, each curve corresponds to a different ϵ in Cox's theory. However, the individual ratios of $\epsilon_{grid} = \frac{\Delta x}{R}$ and the ϵ_{Cox} of the fitted curve appear to remain constant with-in each graph. This result suggests that with a different choice of the shear model it may be possible to get grid independence. As expected, discrepancy appears between the angles predicted by the numerical simulations and Cox's theory when the Ca is large. This regime is where Cox's theory starts to break down since it assumed that $Ca < 1$.

6 Conclusion

A new numerical framework based on the filtered Navier-Stokes equations is proposed for the simulation of the contact line problem. Two unclosed terms are identified, namely an unresolved curvature and the filtered wall shear stress. Models have been proposed for both terms. The model for the unresolved curvature at the wall κ_{unr} appears to capture most of the characteristics present in the model proposed by Cox [1]. However, there is a grid dependence which appears to occur due to the lack of an explicit presence of the slip length in the numerical implementation. This grid dependence certainly has some of its origins in the simple choice of a shear model used for the viscous dissipation at the wall. In order to achieve grid independence and capture the physics at the contact line completely, an alternative model for the shear force at the wall would need to be proposed.

This material is based upon work supported by the National Science Foundation Graduate Research Fellowship under Grant No. DGE-1144469.

References

[1] R. G. Cox. The dynamics of the spreading of liquids on a solid surface. part 1. viscous flow. J. Fluid Mech., 168:169–194, 1986.

[2] C. Huh and L. E. Scriven. Hydrodynamic model of steady movement of a solid / liquid / fluid contact line. J. Colloid Inter. Sci., 35:85–101, 1971.

[3] E. B. Dussan. On the spreading of liquids on solid surfaces: static and dynamic contact lines. Ann. Rev. Fluid Mech., 11:371–400, 1979.

[4] T. D. Blake. The physics of moving wetting lines. J. Colloid Inter. Sci., 299:1–13, 2006.

[5] H. Liu, S. Krishnan, S. Marella, and H. S. Udaykumar. Sharp interface cartesian grid method ii: a technique for simulating droplet interactions with surfaces of arbitrary shape. J. Comput. Phys., 210:32–54, 2005.

[6] P. D. M. Spelt. A level-set approach for simulations of flows with multiple moving contact lines with hysteresis. J. Comput. Phys., 207:389–404, 2005.

[7] P. D. M. Spelt. Shear flow past two-dimensional droplets pinned or moving on an adhering channel wall at moderate reynolds numbers: a numerical study. J. Fluid Mech., 561:439–463, 2006.

[8] P. A. Thompson and M. O. Robbins. Simulations of contact-line motion: slip and the dynamic contact angle. Phys. Rev. Lett., 63:766–769, 1989.

[9] P. A. Thompson and S. M. Troian. A general boundary condition for liquid flow at solid surfaces. Nature, 389:360–362, 1997.

[10] S. H. Davis. Interfacial fluid dynamics. In G. K. Batchelor, H. K. Moffatt, and M. G. Worster, editors, Perspectives in Fluid Dynamics, chapter 1. Cambridge University Press, 2000.

[11] R. L. Hoffman. A study of the advancing interface i. interface shape in liquid-gas systems. J. Colloid Inter. Sci., 50:228–241, 1975.

[12] P. Sheng and M. Zhou. Immiscible-fluid displacement: contact-line dynamics and the velocity-dependent capillary pressure. Phys. Rev. A, 45:5694–5708, 1992.

[13] Š. Šikalo, H. D. Wilhelm, I. V. Roisman, S. Jakirlić, and C. Tropea. Dynamic contact angle of spreading droplets: experiments and simulations. Phys. Fluids, 17, 2005.

[14] S. Afkhami, S. Zaleski, and M. Bussman. A mesh-dependent model for applying dynamic contact angles to vof simulations. J. Comput. Phys., 228:5370–5389, 2009.

[15] R. Scardovelli and S. Zaleski. Direct numerical simulation of free-surface and interfacial flow. Ann. Rev. Fluid Mech., 31:567–603, 1999.

[16] M. Renardy, Y. Renardy, and J. Li. Numerical simulation of moving contact line problems using a volume-of-fluid method. J. Comput. Phys., 171:243–263, 2001.

[17] S. Unverdi and G. Tryggvason. A front-tracking method for viscous incompressible multi-fluid flows. J. Comput. Phys., 100:25–37, 1992.

[18] S. Osher and R. Fedkiw. Level Set Methods and Dynamic Implicit Surfaces. Springer, 2003.

[19] D. Enright, R. Fedkiw, J. Ferziger, and I. Mitchell. A hybrid particle level set method for improved interface capturing. J. Comput. Phys., 183:83–116, 2002.

[20] M. Sussman and E. G. Puckett. A coupled level set and volume of fluid method for computing 3d and axisymmetric incompressible two-phase flows. J. Comput. Phys., 162:301–337, 2000.

[21] E. Olsson and G. Kreiss. A conservative level set method for two phase flow. J. Comput. Phys., 210:225–246, 2005.

[22] D. Hartmann, M. Meinke, and W. Schröer. The constrained reinitialization equation for level set methods. J. Comput. Phys., 229:1514–1535, 2010.

[23] L. D. Landau and E. M. Lifshitz. Fluid Mechanics. Pergamon Press, 1982.

[24] O. Desjardins, G. Blanquart, G. Balarac, and H. Pitsch. High order conservative finite difference scheme for variable density low mach number turbulent flows. J. Comput. Phys., 227:7125–7159, 2008.

[25] O. Desjardins and H. Pitsch. A spectrally refined interface approach for simulating multiphase flows. J. Comput. Phys., 228:1658–1677, 2009.

[26] J. Kim and P. Moin. Application of a fractional-step method to incompressible navier-stokes equations. J. Comput. Phys., 59:308–323, 1985.

[27] R. Fedkiw, T. Aslam, B. Merriman, and S. Osher. A non-oscillatory eulerian approach to interfaces in multimaterial flows (the ghost fluid method). J. Comput. Phys., 152:457–492, 1999.

[28] M. Kang, R. P. Fedkiw, and X. Liu. A boundary condition capturing method for multiphase incompressible flow. J. Sci. Comput., 15:323–360, 2000.

[29] M. Sussman, K. M. Smith, M. Y. Hussaini, M. Ohta, and R. Zhi-Wei. A sharp interface method for incompressible two-phase flows. J. Comput. Phys., 221:469–505, 2007.

[30] D. Bonn, J. Eggers, J. Indekeu, J. Meunier, and E. Rolley. Wetting and spreading. Rev. Mod. Phys., 81:739–805, 2009.

[31] A. Theodorakakos, T. Ous, M. Gavaises, J. M. Nouri, N. Nikolopoulos, and H. Yanagihara. Dynamics of water droplets detached from porous surfaces of relevance to pem fuel cells. J. Colloid Inter. Sci., 300:673–687, 2006.

[32] F. Gibou, R. Fedkiw, L.-T. Cheng, and M. Kang. A second order accurate symmetric discretization of the poisson equation on irregular domains. J. Comput. Phys., 176:205–227, 2002.